tvst

Article

Visible-Light Optical Coherence Tomography Fibergraphy for Quantitative Imaging of Retinal Ganglion Cell Axon Bundles

David A. Miller[1,*], Marta Grannonico[2,*], Mingna Liu[2], Roman V. Kuranov[1,3], Peter A. Netland[4], Xiaorong Liu[2,5], and Hao F. Zhang[1,6]

[1] Department of Biomedical Engineering, Northwestern University, Evanston, IL, USA
[2] Department of Biology, University of Virginia, Charlottesville, VA, USA
[3] Opticent Health, Evanston, IL, USA
[4] Department of Ophthalmology, University of Virginia, Charlottesville, VA, USA
[5] Department of Psychology, University of Virginia, Charlottesville, VA, USA
[6] Department of Ophthalmology, Northwestern University, Evanston, IL, USA

Correspondence: Xiaorong Liu, Department of Biology, University of Virginia, Charlottesville, 485 McCormick Road, Gilmer Hall 480, VA 22903, USA. e-mail: xl8n@virginia.edu
Hao F. Zhang, Department of Biomedical Engineering, Northwestern University, 2145 Sheridan Road, Tech M335, Evanston, IL 60208, USA. e-mail: hfzhang@northwestern.edu

Received: February 25, 2020
Accepted: September 18, 2020
Published: October 9, 2020

Keywords: optical coherence tomography; ganglion cell axon bundles; image analysis

Citation: Miller DA, Grannonico M, Liu M, Kuranov RV, Netland PA, Liu X, Zhang HF. Visible-light optical coherence tomography fibergraphy for quantitative imaging of retinal ganglion cell axon bundles. Trans Vis Sci Tech. 2020;9(11):11, https://doi.org/10.1167/tvst.9.11.11

Purpose: To develop a practical technique for visualizing and quantifying retinal ganglion cell (RGC) axon bundles in vivo.

Methods: We applied visible-light optical coherence tomography (vis-OCT) to image the RGC axon bundles, referred to as vis-OCT fibergraphy, of healthy wild-type C57BL/6 mice. After vis-OCT imaging, retinas were flat-mounted, immunostained with anti-beta-III tubulin (Tuj1) antibody for RGC axons, and imaged with confocal microscopy. We quantitatively compared the RGC axon bundle networks imaged by in vivo vis-OCT and ex vivo confocal microscopy using semi-log Sholl analysis.

Results: Side-by-side comparison of ex vivo confocal microscopy and in vivo vis-OCT confirmed that vis-OCT fibergraphy captures true RGC axon bundle networks. The semi-log Sholl regression coefficients extracted from vis-OCT fibergrams (3.7 ± 0.8 mm^{-1}) and confocal microscopy (3.6 ± 0.3 mm^{-1}) images also showed good agreement with each other ($n = 6$).

Conclusions: We demonstrated the feasibility of using vis-OCT fibergraphy to visualize RGC axon bundles. Further applying Sholl analysis has the potential to identify biomarkers for non-invasively assessing RGC health.

Translational Relevance: Our novel technique for visualizing and quantifying RGC axon bundles in vivo provides a potential measurement tool for diagnosing and tracking the progression of optic neuropathies.

Introduction

Optical coherence tomography (OCT) is a non-invasive imaging technology that detects backscattered light to form high-resolution, three-dimensional (3D) images of living retinas.[1] After it was first developed, OCT quickly became the clinical standard for identifying and diagnosing morphological indicators for optic neuropathies.[2] Current clinical diagnostic techniques involve retinal nerve fiber layer (RNFL) thickness measurements as a major indicator for

neuronal loss[3–5]; however, this thickness measurement may vary due to differences in axial resolution and segmentation algorithms of different OCT systems.[6] Furthermore, current diagnostic techniques overlook the topographic organization of the retinal ganglion cell (RGC) axon bundles which may provide additional details to aid in the diagnosis of optic neuropathies. Techniques that have been introduced for visualizing the topographic organization of the RGC axon bundle network make use of spectral-domain OCT, adaptive optics OCT, and confocal scanning laser ophthalmoscopy. However, these techniques for visualizing the RGC axon bundles require injection of exogenous contrast agents,[7] long acquisition times,[8] or sensitive hardware components,[9,10] making them less than ideal for large-scale animal studies or widespread clinical use.

In this study, we introduce visible-light OCT (vis-OCT) fibergraphy, an en face visualization of the RGC axon bundles, and an analytic technique, based on semi-log Sholl analysis, to quantify overall RGC axon bundle organization. We validate in vivo vis-OCT fibergrams and their corresponding RGC axon bundle organization by comparing them with ex vivo confocal microscopy images of the same retinas after being flat-mounted and immunostained with anti-beta-III tubulin (Tuj1) to indicate RGC axons. Our results indicate that in vivo vis-OCT fibergraphy is highly consistent with ex vivo confocal microscopy results.

Methods

Animal protocols were approved by the institutional animal care and use committees of Northwestern University and the University of Virginia. All protocols complied with the ARVO Statement for the Use of Animals in Ophthalmic and Vision Research and National Institutes of Health guidelines.

Animal Preparation

Healthy 2- to 4-month-old wild-type C57BL/6 mice (The Jackson Laboratory, Bar Harbor, ME) were used. Prior to vis-OCT imaging, mice were anesthetized by an intraperitoneal injection of a mixture of ketamine (114 mg/kg; Henry Schein Animal Health, Dublin, OH) and xylazine (17 mg/kg; Akorn, Inc., Lake Forest, IL). The pupils were dilated using tropicamide drops (1%; Henry Schein Animal Health). During imaging, mice were kept warm with an infrared lamp, and polyvinyl alcohol artificial tear drops (1.4%; Rugby Laboratories, Inc., Hempstead, NY) were given after each image acquisition to prevent corneal dehydration.

Visible-Light Optical Coherence Tomography

We imaged the mice using a commercial small-animal vis-OCT system (Halo 100; Opticent Health, Evanston, IL) as illustrated in Figure 1. This system used a supercontinuum light source (SuperK EXW-6; NKT Photonics, Birkerød, Denmark), which was filtered with a dichroic mirror to deliver visible-light illumination between 480 nm and 650 nm. The illumination light was launched to a 2 × 2 fiber coupler, which divided the light to the reference and sample arms. The sample arm consisted of a pair of galvanometer scan mirrors and a 3:1 Keplerian telescope system. The power incident on the cornea was 1 mW. The reference arm consisted of a polarization controller and glass plates for dispersion compensation. The returned interference fringes were recorded using a commercial spectrometer designed for vis-OCT (Blizzard SR; Opticent Health). We used an A-line rate of 25 kHz and an integration time of 39.3 µs per A-line. The spectral detection range of the spectrometer was between 508 nm and 613 nm, which provided an axial resolution of 1.3 µm in the retina. According to our simulation, the lateral resolution was between 4.5 µm at the center of the field of view and 8.7 µm at 350 µm from the center. The total imaging volume was approximately 700 µm (x) × 700 µm (y) × 1500 µm (z).

For each mouse, we acquired four vis-OCT volumes (512 A-lines/B-scan, 512 B-scans/volume) from the same eye with the optic nerve head (ONH) aligned in the four corners of the field of view to cover different areas of the retina. Such placement minimized the retinal curvature, which maximized RNFL reflectance throughout the field of view. After fibergram processing, we montaged the four images acquired from each mouse. On average, the final montaged images were approximately 1.2 mm (x) × 1.2 mm (y). Each OCT volume was acquired in 10.5 seconds and required about 1 minute to reposition the eye between acquisitions.

For demonstration, vis-OCT angiography (OCTA) was used to contrast the blood vessels from the RGC axon bundles. Each B-scan was repeated five times to detect phase differences indicating blood flow. Our protocol to extract the OCTA signal was described previously.[11] The acquisition time for a single OCTA volume was 52.4 seconds.

Vis-OCT Fibergram Processing

We processed the vis-OCT volumes using background subtraction, numerical dispersion compensation, k-space resampling, and B-scan registration, as previously reported.[12] To isolate the RNFL,

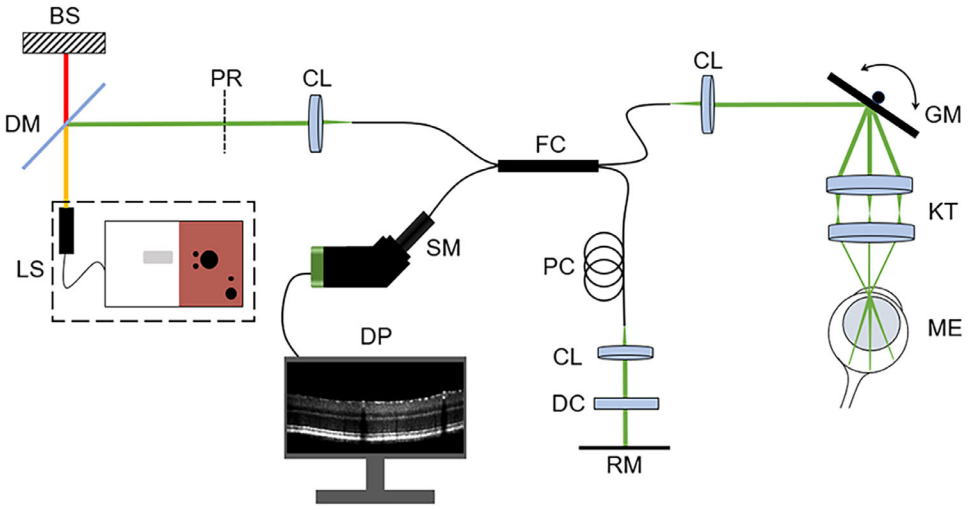

Figure 1. Schematic of the small-animal vis-OCT system. BS, beams stop; DC, dispersion compensation; DM, dichroic mirror; DP, data processing; FC, 2 × 2 fiber coupler; GM, galvanometer scan mirrors; KT, Keplerian telescope; LS, supercontinuum light source; ME, mouse eye; PC, polarization controller; PR, polarizer; RM, reference mirror; SM, spectrometer.

we used threshold-based surface segmentation to crop a rectangular slab ~26 µm thick from the top surface of the retina. Figure 2a shows the region selected by the segmentation algorithm (red lines), and Figure 2b shows the resulting slab.

Taking advantage of the strong backscattering nature of the RGC axon bundles and blood vessels, we used spectroscopic segmentation to isolate the RGC axon bundles and blood vessels from surrounding tissues. We performed a short-time Fourier transform (STFT) using 24 Gaussian windows equally spaced in wavenumber with an equivalent bandwidth of 11 nm at 560 nm. Doing so reduced the axial resolution to ~12.6 µm. As illustrated in Figure 2c, we reconstructed the B-scans for each wavelength and cropped the same ~26 µm-thick rectangular slab from the surface of the retina. We then calculated the mean intensity spectrum within the cropped RNFL region and subtracted the mean at each pixel. This difference was then summed across the spectrum to yield a single difference from mean (DiFM) value for each pixel. Pixels with a higher DiFM indicate higher backscattering than surrounding tissues.[13] This process is summarized as

$$DiFM(x, y, z) = \sum_{\lambda=1}^{\lambda_n} \left[\bar{I}_{RNFL}(\lambda) - I(x, y, z, \lambda)\right] \quad (1)$$

where $\bar{I}_{RNFL}(\lambda)$ indicates the mean intensity within the cropped RNFL region for a given wavelength λ; and $I(x, y, z, \lambda)$ is the intensity of a pixel at a given wavelength. Figure 2d shows the DiFM image of the cropped region. As illustrated in Figure 2e, we used the segmentation to create a 3D binary mask, which we applied to the cropped vis-OCT B-scans. The segmented RNFL en face image was generated by averaging the 3D volume along the depth direction, as shown in Figure 2f.

After processing the OCTA volumes, we used threshold-based segmentation to isolate the superficial capillary plexus (SCP) and deep capillary plexus (DCP). As depicted in Figure 2g, we segmented the SCP (red lines) from the RNFL to the inner plexiform layer.[14] We created en face images of the SCP (Fig. 2h) and DCP (Fig. 2i) by taking the maximum intensity projection of each cropped volume. Finally, the vis-OCT fibergram image (green channel) was combined with SCP (red channel) and DCP (blue channel) to form an RGB image. Figure 2j shows the combined image.

Immunostaining and Confocal Microscopy

Immediately after acquiring vis-OCT data, we euthanized the mice with Euthasol (15.6 mg/mL; Virbac Corp., Westlake, TX) and perfused them with 4% paraformaldehyde (PFA) in phosphate-buffered saline. The eyes were enucleated, and a mark was made on the temporal side to indicate orientation. After carefully removing the anterior chamber, ocular lens, and vitreous, the eyecups were further fixed in PFA for 30 minutes. The eyecups were then blocked in 5% donkey serum with 2.5% bovine serum albumin and 0.5% Triton X-100 in Tris-buffered saline (pH 7.5) for 2 hours at room temperature. The primary antibody, anti-Tuj1 (1:200; a gift from Anthony J. Spano), was incubated overnight at 4°C, and secondary antibody,

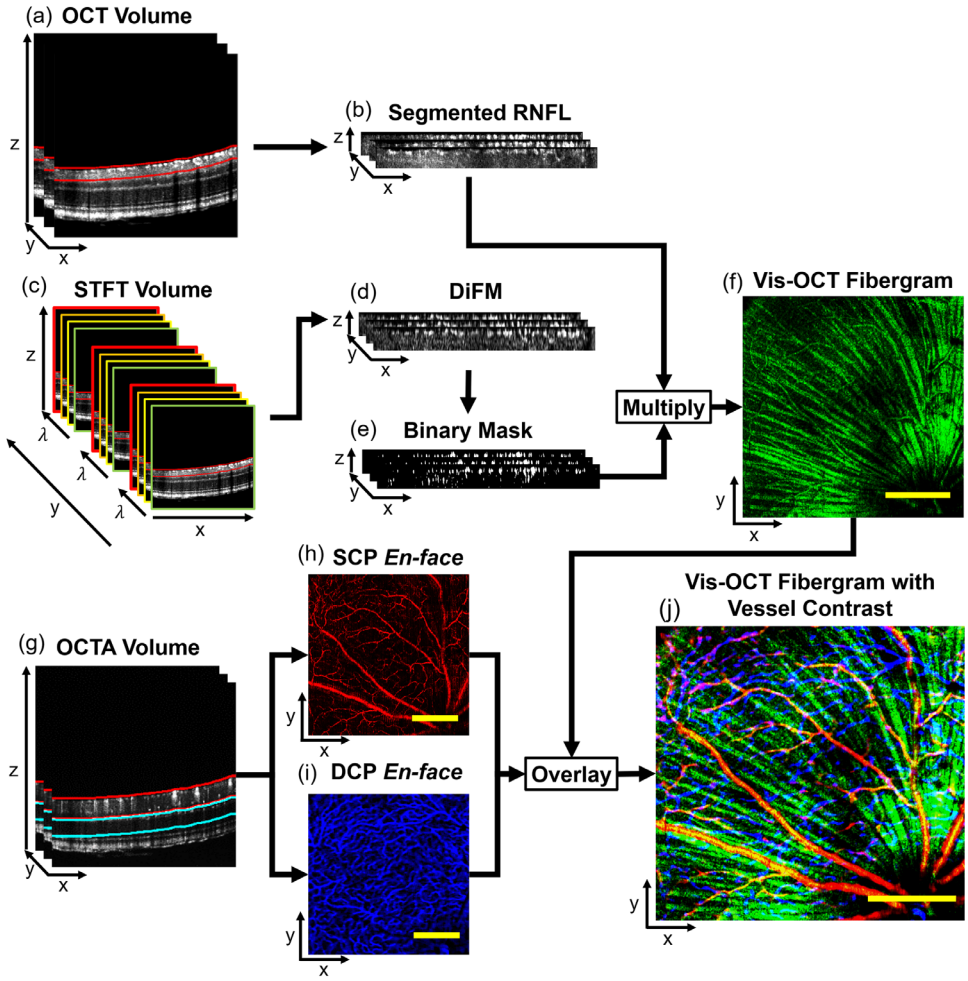

Figure 2. Data processing flowchart for vis-OCT fibergraphy. (a) RNFL (*red lines*) is segmented from the OCT volume. (b) Slab ~26 µm thick containing the RNFL after segmentation from the OCT volume. (c) STFT is applied and B-scans are reconstructed for each wavelength to create the STFT volume; the RNFL is segmented (*red lines*) from the STFT volume to create an ~26-µm-thick spectroscopic RNFL volume. (d) DiFM is calculated from the spectroscopic RNFL volume. (e) Binary mask is generated by thresholding the DiFM volume. (f) Binary mask is multiplied with the segmented RNFL, and the vis-OCT fibergram is generated by mean intensity projection. (g) The SCP (*red lines*) and DCP (*blue lines*) are segmented from the OCTA volume. (h) SCP en face image created by maximum intensity projection of region segmented in (g). (i) DCP en face image created by maximum intensity projection of region segmented in (g). (j) Blood vessels are contrasted from the vis-OCT fibergram by combining the vis-OCT fibergram (*green channel*), SCP (*red channel*), and DCP (*blue channel*) en face images in an RGB image. *Scale bars*: 150 µm.

Donkey anti-Mouse Immunoglobulin G conjugated to Alexa Fluor 488 (1:1000; Thermo Fisher, Scientific, Waltham, MA), was incubated overnight at 4°C. The retinas were flat-mounted and coverslipped with VECTASHIELD mounting medium (Vector Laboratories, Inc., Burlingame, CA).

Confocal microscopy was performed using the 3D Z-stack mode on a Zeiss LSM 800 microscope (Carl Zeiss Meditec AG, Oberkochen, Germany). At least 25 tiles across the whole retina were imaged to cover the total volume of 5.99 mm (x) × 5.88 mm (y) × 30 µm (z) at a pixel size of 1.24 µm/pixel. Z-stack slices were then projected to create two-dimensional en face confocal microscopy images.

RGC Axon Bundle Analysis

We developed a technique, based on semi-log Sholl analysis,[15] to quantify the overall organization of RGC axon bundles. This technique consists of drawing concentric circles centered on the ONH and counting the number of RGC axon bundle intersections (N) with circles of increasing radius (r). The number of intersections at each radius is normalized by the circle area

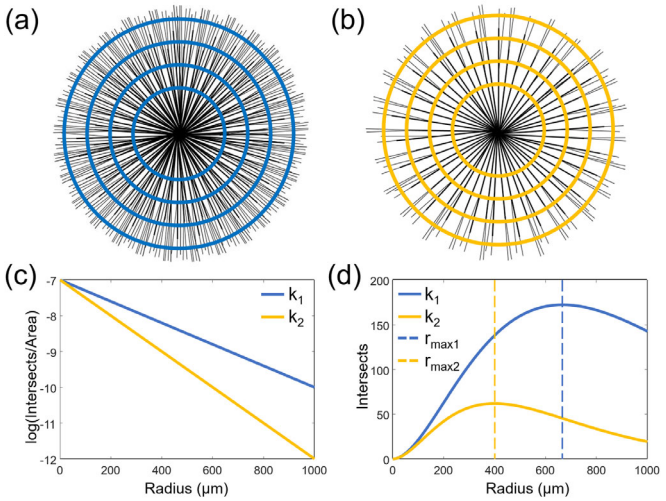

Figure 3. RGC axon bundle organization analysis. (a) Illustration of the retina with high RGC axon bundle density. (b) Illustration of the retina with low RGC axon bundle density. (c) The semi-log relationship between RGC axon bundle intersections and radius. (d) RGC axon bundle intersections as a function of radius. k_1, high density; k_2, low density.

(A) and plotted on a semi-log axis. We then fit a first-order polynomial to the generated plot, which follows the relationship described in Equation 2, where k is the Sholl regression coefficient and m is the intercept:

$$\log\left(\frac{N}{A}\right) = -kr + m. \tag{2}$$

The Sholl regression coefficient can be considered as a measure of the rate of change in RGC axon bundle density as a function of distance from the ONH. Figures 3a and 3b illustrate RGC axon bundle structures with high and low bundle densities, respectively. The high-density RGC axon bundle structure corresponds to a lower Sholl regression coefficient (k_1), demonstrated by the slope of the blue line in Figure 3c. Conversely, the RGC axon bundle structure with lower density corresponds to a higher Sholl regression coefficient (k_2) because the density of the RGC axon bundles decreases more rapidly away from the ONH compared to the RGC axon bundle structure with higher density. This faster decrease is depicted by the slope of the yellow line in Figure 3c. Using the Sholl regression coefficients, the number of intersections can be plotted as a function of radius, as shown in Figure 3d. The radius at which the number of RGC axon bundle intersections reaches a maximum is the maximum intersection radius ($r_{max} = 2/k$). The maximum intersection radius, indicated by the dashed vertical lines in Figure 3d, is higher for retinas with higher bundle density (r_{max1}) and lower for retinas with lower bundle density (r_{max2}).

We automated this process to quantify the RGC axon bundles in the confocal microscopy and vis-OCT fibergram images. To do so, we applied a Gaussian filter to the image and manually selected a point at the center of the ONH. To ensure that the area of the analysis was the same for corresponding confocal images and vis-OCT fibergrams, we selected the same point on the ONH using common retinal features as reference points. We then mapped a circle with a 225-μm radius centered on the ONH and plotted the pixel intensity values about the circle. We selected an initial radius of 225 μm because this is the approximate radius at which the RGC axon bundles are distinguishable from each other. The number of intensity peaks was used as the number of RGC axon bundle intersections. For this study, we did not remove the blood vessels for the vis-OCT Sholl regression coefficient estimation. This is because the number of blood vessels is significantly less than the number of RGC axon bundles, which adds negligible error to the estimation of the Sholl regression coefficient. We reiterated the process, incrementing the radius by 1 pixel, until the circle reached a radius of 425 μm on the fundus image.

Due to variations in optical focus in mouse eyes and the lower lateral resolution of OCT compared to confocal microscopy, we found that some of the Sholl regression coefficient estimates may be less reliable for vis-OCT fibergrams. To assess the reliability of the Sholl regression coefficient estimate, we measured the acutance[16] of the confocal microscopy images and vis-OCT fibergrams. The acutance estimates the perceived image sharpness based on the edge contrast of the image. In other words, a higher acutance value indicates that the image is focused well and the Sholl regression coefficient estimate is more reliable. The acutance can be described by

$$S = \frac{1}{N}\sum_{x_i}\sum_{y_i}\sqrt{G_x^2 + G_y^2}\,, \tag{3}$$

where S is the image acutance; N is the total number of image pixels; x_i is the horizontal pixel index; y_i is the vertical pixel index; G_x is the horizontal image gradient; and G_y is the vertical image gradient.

Statistical Analysis

We used paired t-tests to calculate the statistical difference between confocal and vis-OCT data. To quantify the difference between the results for confocal microscopy and vis-OCT fibergram images,

we calculated the percent difference (PD) defined by

$$PD = \frac{|x_c - x_o|}{(x_c + x_o)/2}, \quad (4)$$

where x_c is the confocal microscopy Sholl regression coefficient or acutance, and x_o is the vis-OCT fibergram Sholl regression coefficient or acutance.

Results

Comparing Confocal Microscopy and Vis-OCT Fibergraphy

We imaged the retinas of six healthy wild-type mice using vis-OCT fibergraphy and montaged the fibergrams (Fig. 4a). To demonstrate the level of detail achieved by vis-OCT fibergraphy, we compared the montaged vis-OCT fibergrams with their corresponding confocal images of immunostained flat-mounted retinas to indicate RGC axons (Fig. 4b). We divided the full retina images into superior (S), inferior (I), nasal (N), and temporal (T) quadrants, as highlighted in Figures 4a and 4b. Figures 4c and 4d are magnified views of the areas highlighted in Figures 4a and 4b, respectively. The orange arrows (labeled 1 to 4) highlight four small axon bundles visible in both vis-OCT fibergraphy and confocal microscopy corresponding to the diameters of (1) 7.9 µm, (2) 6.4 µm, (3) 2.5 µm, and (4) 6.5 µm quantified by confocal microscopy. This result validates the capability of vis-OCT fibergraphy to resolve individual RGC axon bundles with varying sizes in vivo. The red arrows (labeled 5 to 7) highlight blood vessels visible in vis-OCT fibergraphy but which appear as dark shadows in confocal microscopy. Figure 4e shows the vis-OCT fibergram for a single vis-OCT volume outlined by the yellow dashed box in Figure 4a. Figure 4f shows a B-scan reconstructed from the red arc in Figure 4e. As indicated by the orange arrows, the RGC axon bundles form a single layer on the inner surface of the mouse retina. The red arrows in Figure 4f indicate blood vessels, which form dark shadows through all layers of the retina beneath them.

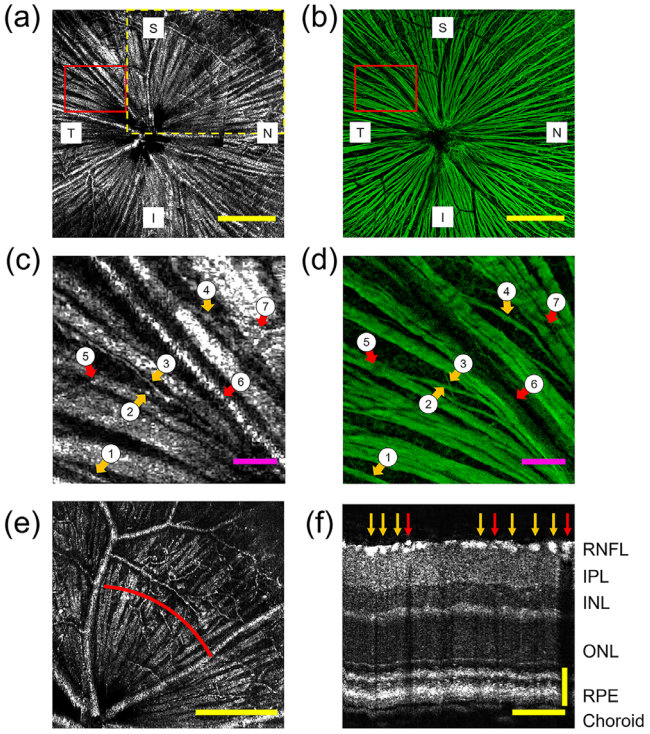

Figure 4. Comparing vis-OCT fibergraphy and confocal microscopy RGC axon bundle images. (a) In vivo vis-OCT fibergram. (b) Ex vivo confocal microscopy image of the immunostained flat-mounted retina. *Scale bars*: 250 µm. (c) Magnified view of the highlighted area in (a). (d) Magnified view of highlighted area in (b). The *orange arrows* (1 to 4) indicate four small RGC axon bundles visible in both vis-OCT fibergrams and confocal microscopy images. The *red arrows* (5 to 7) indicate blood vessels. *Scale bars*: 50 µm. (e) Fibergram from a single OCT volume indicated by the *dashed yellow box* in (a). *Scale bar*: 250 µm. (f) B-scan image reconstructed from *red arc* shown in (e) centered 400 µm from the ONH. The *orange arrows* indicate RGC axon bundles (*bright spots*) and the *red arrows* indicate blood vessels (*dark shadows* through all subsequent layers). IPL, inner plexiform layer; INL, inner nuclear layer; ONL, outer nuclear layer; RPE, retinal pigment epithelium. *Scale bars*: 100 µm horizontal, 50 µm vertical.

Structural Analysis of RGC Axon Bundles

We performed semi-log Sholl analysis to compare the overall RGC axon bundle networks from the montaged vis-OCT fibergram images and their corresponding confocal microscopy images. Figures 5a and 5b show the semi-log Sholl regression plots for the vis-OCT fibergraphy and confocal microscopy images shown in Figures 4a and 4b, respectively. The plot points indicate the measured $\log(N/A)$ values at each radius, and the solid line indicates the first-order polynomial fit. The average Sholl regression coefficients were 3.7 ± 0.8 mm^{-1} for vis-OCT fibergraphy and 3.6 ± 0.3 mm^{-1} for confocal microscopy images ($n = 6$). We found no significant difference between the Sholl regression coefficients for in vivo vis-OCT fibergraphy and ex vivo confocal microscopy ($P = 0.66$, t-test). The average acutance values were 0.044 ± 0.009 for vis-OCT fibergraphy and 0.067 ± 0.003 for confocal microscopy. There was a significant difference between the acutance values for vis-OCT fibergraphy and confocal microscopy ($P = 0.002$, t-test). The Sholl regression coefficient, acutance and percent difference values for each eye are given in the Table.

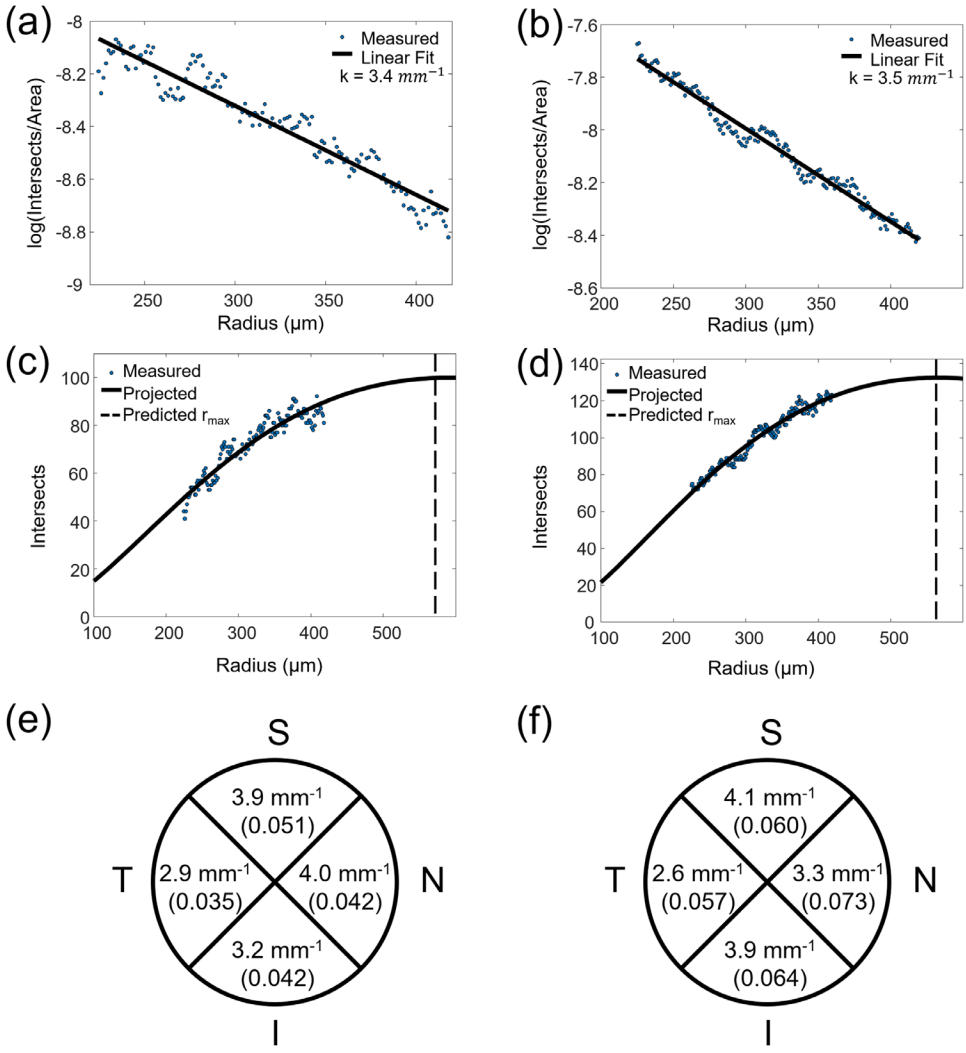

Figure 5. RGC axon bundle quantifications. (a) Semi-log Sholl regression plot for in vivo vis-OCT fibergram shown in Figure 4a. (b) Semi-log Sholl regression plot for ex vivo confocal microscopy image shown in Figure 4b. (c) Plot of vis-OCT fibergram intersections for fibergram shown in Figure 4a. (d) Plot of confocal microscopy intersections for retina shown in Figure 4b. (e) Vis-OCT Sholl regression coefficients and acutance values for each retinal quadrant for fibergram shown in Figure 4a. (f) Confocal microscopy Sholl regression coefficients and acutance values for each retinal quadrant shown in Figure 4b.

Following the intersections analysis illustrated in Figure 3d, we used the Sholl regression coefficients to determine the maximum intersection radius (r_{max}) for the vis-OCT fibergrams and confocal microscopy images shown in Figures 5c and 5d, respectively. The plot points indicate the measured number of RGC axon bundle intersections at each radius. The solid line indicates the projected number of intersections at each radius as a continuous function derived from the first-order polynomial fit parameters. The vertical dashed lines indicate the predicted r_{max}. The average r_{max} was 553 ± 96 μm for vis-OCT fibergrams and 558 ± 48 μm for confocal microscopy ($n = 6$), showing no significant difference between the two ($P = 0.91$, t-test). The r_{max} values for all eyes are listed in the Table.

For the eye with the lowest overall percent difference between confocal and vis-OCT Sholl regression coefficients (mouse 4 in the Table), we investigated how the Sholl regression coefficient varied in each quadrant of the retina, as shown in Figures 5e and 5f. The Sholl regression coefficient percent difference was lowest in the superior quadrant (4%) and highest in the nasal quadrant (19%). To investigate the source of this large percent difference, we compared the acutance value for each quadrant. Following the same trend as the Sholl regression coefficient percent

Table. Summary of RGC Axon Bundle Image Analysis Results

	Vis-OCT			Confocal Microscopy			Percent Difference (%)[a]	
	k (mm^{-1})	r_{max} (μm)	S	k (mm^{-1})	r_{max} (μm)	S	k	S
Mouse								
1	3.3	612	0.053	3.9	512	0.063	18	17
2	4.0	504	0.038	3.4	590	0.066	16	54
3	5.2	386	0.032	3.8	521	0.067	30	71
4	3.4	592	0.042	3.5	565	0.064	5	41
5	3.1	654	0.050	3.8	526	0.070	22	35
6	3.5	570	0.052	3.2	635	0.070	11	29
Mean	3.7	553	0.044	3.6	558	0.067	17	41
SD	0.8	96	0.009	0.3	48	0.003	9	19

[a]Mean and standard deviation values in percent difference column refer to mean and standard deviation of percent difference values.

difference, the acutance percent difference was lowest in the superior quadrant (18%) and highest in the nasal quadrant (55%). The acutance values for each quadrant are indicated beneath the Sholl regression coefficients in Figures 5e and 5f.

Discussion and Conclusions

In this work, we presented an imaging methodology referred to as vis-OCT fibergraphy. It provides an en face visualization of the RGC axon bundle network and can be integrated with OCTA to visualize simultaneously acquired surrounding vasculature in vivo. We further introduced a novel technique to characterize the RGC axon bundle network organization using Sholl analysis. Combining vis-OCT fibergraphy and Sholl analysis builds the foundation for a potential tool for non-invasively monitoring RGC health. In humans, such a tool has the potential to detect minute structural damage associated with optic neuropathies, such as glaucoma, prior to substantial RGC loss.

Side-by-side comparison between ex vivo confocal microscopy and in vivo vis-OCT fibergraphy revealed identical RGC axon bundle networks from the same retinas. The measured Sholl regression coefficients were not significantly different between in vivo and ex vivo measurements. These results confirm that vis-OCT fibergraphy could serve as a suitable method for visualizing RGC axon bundles in vivo. Additionally, the Sholl analysis results identified the same RGC axon bundle density in vivo and ex vivo. Such analysis could potentially serve as an indicator for optic neuropathies upon further validation in disease models.

Analysis of the Sholl regression coefficient revealed large percent differences between in vivo vis-OCT fibergrams and ex vivo confocal microscopy images in different retinal quadrants. Image sharpness analysis showed that such differences were largely due to reduced image quality in the vis-OCT images caused by optical defocusing. To correct for this, we propose implementing a quality metric to guide image acquisition.[17] Additional techniques, such as computational adaptive optics, could be applied to further enhance focus after acquisition.[18,19] Another source of error is associated with histological preparation, which may change the RGC axon bundle size and orientation.

Many studies have monitored RGC axon bundle health in primates,[20,21] rodents,[22–24] and human patients.[25–27] In isolated rat retinas, optical properties, such as the RNFL reflectance spectrum and birefringence, were found to be different following chronic ocular hypertension.[24] In vivo monitoring of the changes of axon bundle structure became possible in recent years. For example, confocal scanning laser ophthalmoscopy was used to monitor RGC axon bundles after optic nerve crush injury in rat.[7] To do so, the RGC axon bundles were labeled with fluorescent dyes via intravitreal injections; however, the fluorescent dyes decrease in intensity over time and cannot be repeatedly taken up by the same RGC axon bundles of interest, and the dye labels only a sparse subset of RGC axons. Vis-OCT fibergraphy does not require injection of any contrast agent or other invasive procedures, making it more suitable for longitudinal in vivo studies and clinical applications.

Many other techniques have also been proposed to quantify organizations of biological network-like structures, such as the RGC axon bundle network. Fractal analysis has been used to characterize neurons based on how completely they fill up an area. For example, a highly branching structure on a two-dimensional plane will have a fractal dimension closer to two. This technique has the advantage of being scale invariant with less variability among subjects, but it does not provide the most intuitive or precise output.[28] Other methods applied specifically to the analysis of RGC axon bundles in human include spatial density analysis,[7,29] lateral bundle thickness measurements,[30] and RGC axon bundle trajectory mapping.[9,31] These techniques have the advantage of being more precise and intuitive but can have greater variability among subjects. The RGC axon bundles are radially organized such that the bundle density is higher near the ONH and lower at the periphery. Because of this, the density varies as a function of distance from the ONH; therefore, parameters such as density and the raw number of bundles measured uniformly or at a fixed distance from the ONH do not adequately describe the overall organization. We selected the semi-log Sholl analysis because it describes how the density changes with distance from the ONH.

Extensive evidence suggests that neurons have distinct classes of self-destructive programs that are spatially compartmentalized.[32,33] RGCs receive synaptic inputs through their dendritic trees in the inner plexiform layer and send the output to higher visual centers in the brain via their axons.[34,35] RGC axon pathfinding during early development has been studied for decades, revealing that many molecules are responsible for bundle formation, axon guidance, and pathfinding from the RGC soma to the ONH and specific brain regions.[36,37] In various neurodegenerative diseases, axons and dendrites often degenerate prior to cell death, which might be an important clinical feature for early detection of neuronal loss.[32,38]

For example, damages in the RGC axons in the ONH can be associated with early pathophysiology underlying glaucomatous neuronal loss.[39–42] Within individual axons, the cytoskeletal structure, including microtubules and F-actin filaments, shows signs of distortion at early stages of ocular hypertension, which may contribute to changes in RNFL optical properties.[23] The molecular and cellular mechanisms of axon bundle structural changes remain to be fully investigated in disease conditions.[43–45] It has been observed that, as the RGC axon bundles deteriorate, they become thinner and sparser across the retina,[46] which would result in a more rapid change in density away from the ONH and a higher Sholl regression coefficient, corresponding to a lower r_{max}. Therefore, an increasing Sholl regression coefficient over time could be an indicator of dying RGCs.

How the RGC degenerates and dies is not completely understood. Several studies have shown that preventing RGC soma death is not enough to prevent the degeneration of RGC axons.[47] Axonal degeneration was not prevented in mice deficient in the proapoptotic molecule BCL2-associated X protein.[48] On the other hand, in Wallerian degeneration slow (Wld^S) mice, axonal degeneration was significantly slowed while apoptosis occurred normally.[49] Furthermore, RGC loss could be location dependent. For example, we have shown that the superior quadrant of the mouse retina could be susceptible to the insult of sustained ocular hypertension.[50] Jakobs and colleagues[51] showed that RGC loss radiates from the optic nerve head in fan-shaped sectors. The Sholl regression coefficient from different areas or sectors could be used to further determine which retinal quadrant is affected by the disease, as well as its development and progression.

Recently, Pi and colleagues[8] used vis-OCT to image RGC axon bundles, retinal neurons, and retinal vasculature with remarkable detail in rat. This was achieved by combining 110 OCT volumes (512 A-lines × 512 B-scans) acquired over ~26 minutes. Their vis-OCT system is almost identical to the one we describe here, with a spectral detection range of 510 to 610 nm, an axial resolution of 1.2 µm, and a lateral resolution of 6 µm. Here, we have demonstrated that it is possible to visualize the RGC axon bundles in mice using a single OCT volume acquired in 10.5 seconds; this faster acquisition time demonstrates the practicality of vis-OCT fibergraphy for clinical translation and large-scale animal studies. Additionally, we demonstrated the repeatability of vis-OCT fibergraphy by acquiring fibergram images from four different locations in six mouse eyes, and we validated RGC axon bundle organization ex vivo using confocal microscopy. Finally, we have proposed a novel metric for quantifying the organization of the RGC axon bundle network. Overall, the work presented here describes easy-to-replicate techniques for visualizing and quantifying RGC axon bundles in vivo.

We believe that the semi-log Sholl analysis technique could be applied to monitor the health of RGC axon bundles in humans. In human retinas, RGC axon bundles project from the fovea–Bruch's membrane opening axis toward the ONH.[52] Therefore, different retinal landmarks, such as the ONH or fovea, could be selected as the center points for Sholl analysis. We expect the Sholl regression coefficient to be lower at the ONH than the fovea because of the larger density of RGC axon bundles there compared to the fovea. Combining semi-log Sholl analysis with existing diagnostic techniques, such as RNFL thickness measurements and visual field tests, could enable faster detection of optic neuropathies, including glaucoma. However, before implementation in humans, the acquisition speed of vis-OCT will have to be improved to minimize motion and to enable scans with a larger field of view.

In future studies, the simultaneously obtained angiography information, as shown in Figure 2j, could be used to monitor how hemodynamics affect the health of RGC axon bundles. Diabetic retinopathy has been associated with abnormal vascularization, which leads to vision loss.[53] Additionally, studies have shown that the increased intraocular pressure levels associated with glaucoma lead to reduced perfusion of the retina.[54] Therefore, vis-OCT fibergraphy could be applied to investigate what percentage of a decrease in capillary density corresponds to a decrease in RGC axon bundles.

Acknowledgments

The authors thank Lisa Beckmann, Ian Rubinoff, and John Troy for their fruitful discussions.

Supported in part by Grants from the National Institutes of Health (R01EY026078, R01EY029121, R01EY028304, R01EY019949, R01EY026286, and R44EY026466).

Disclosure: **D.A. Miller,** None; **M. Grannonico,** None; **M. Liu,** None; **R.V. Kuranov,** Opticent Health (E); **P.A. Netland,** None; **X. Liu,** None; **H.F. Zhang,** Opticent Health (I)

* DAM and MG contributed equally to this article.

References

1. Huang D, Swanson E, Lin C, et al. Optical coherence tomography. *Science*. 1991;254(5035):1178–1181.
2. Akman A. Role of optical coherence tomography in glaucoma. In: Akman A, Bayer A, Nouri-Mahdavi K, eds. *Optical Coherence Tomography in Glaucoma*. Cham, Switzerland: Springer Nature; 2018:13–25.
3. Davis BM, Crawley L, Pahlitzsch M, Javaid F, Cordeiro MF. Glaucoma: the retina and beyond. *Acta Neuropathol*. 2016;132(6):807–826.
4. Medeiros F, Vizzeri G, Zangwill L, Alencar L, Sample P, Weinreb R. Comparison of retinal nerve fiber layer and optic disc imaging for diagnosing glaucoma in patients suspected of having the disease. *Ophthalmology*. 2008;115(8):1340–1346.
5. Medeiros F, Zangwill L, Anderson D, et al. Estimating the rate of retinal ganglion cell loss in glaucoma. *Am J Ophthalmol*. 2012;154(5):814–824.
6. Dong ZM, Wollstein G, Wang B, Schuman JS. Adaptive optics optical coherence tomography in glaucoma. *Prog Retin Eye Res*. 2017;57:76–88.
7. Kanamori A, Catrinescu M, Traistaru M, Beaubien R, Levin L. In vivo imaging of retinal ganglion cell axons within the nerve fiber layer. *Invest Ophthalmol Vis Sci*. 2010;51(4):2011–2018.
8. Pi S, Hormel T, Wei X, Cepurna W, Morrison J, Jia Y. Imaging retinal structures at cellular-level resolution by visible-light optical coherence tomography. *Optics Lett*. 2020;45(7):2107–2110.
9. Sugita M, Pircher M, Zotter S, et al. Retinal nerve fiber bundle tracing and analysis in human eye by polarization sensitive OCT. *Biomed Opt Express*. 2015;6(3):1030–1054.
10. Kocaoglu O, Cense B, Jonnal R, et al. Imaging retinal nerve fiber bundles using optical coherence tomography with adaptive optics. *Vision Res*. 2011;51(16):1835–1844.
11. Chen S, Liu Q, Shu X, Soetikno B, Tong S, Zhang H. Imaging hemodynamic response after ischemic stroke in mouse cortex using visible-light optical coherence tomography. *Biomed Opt Express*. 2016;7(9):3376–3389.
12. Soetikno B, Beckmann L, Zhang X, Fawzi A, Zhang H. Visible-light optical coherence tomography oximetry based on circumpapillary scan and graph-search segmentation. *Biomed Opt Express*. 2018;9(8):3640–3652.
13. Harper D, Konegger T, Augustin M, et al. Hyperspectral optical coherence tomography for in vivo visualization of melanin in the retinal pigment epithelium. *J Biophotonics*. 2019;12(12):e201900153.
14. Campbell J, Zhang M, Hwang T, et al. Detailed vascular anatomy of the human retina by projection-resolved optical coherence tomography angiography. *Sci Rep*. 2017;7:42201.
15. Sholl D. Dendritic organization in the neurons of the visual and motor cortices of the cat. *J Anat*. 1953;87(4):387–406.
16. Choong Y, Rakebrandt F, North R, Morgan J. Acutance, an objective measure of retinal nerve fibre image clarity. *Br J Ophthalmol*. 2003;87(3):322–326.
17. Stein D, Ishikawa H, Hariprasad R, et al. A new quality assessment parameter for optical coherence tomography. *Br J Ophthalmol*. 2006;90(2):186–190.
18. Adie S, Graf B, Ahmad A, Carney P, Boppart S. Computational adaptive optics for broadband optical interferometric tomography of biological tissue. *Proc Natl Acad Sci USA*. 2012;109(19):7175–7180.
19. Adie S, Shemonski N, Graf B, Ahmad A, Carney P, Boppart S. Guide-star-based computational adaptive optics for broadband interferometric tomography. *Appl Phys Lett*. 2012;101(22):221117.
20. Radius RL, Anderson DR. The histology of retinal nerve fiber layer bundles and bundle defects. *JAMA Ophthalmol*. 1979;97(5):948–950.
21. Quigley HA, Addicks EM. Quantitative studies of retinal nerve-fiber layer defects. *Arch Ophthalmol*. 1982;100(5):807–814.
22. Yi J, Puyang Z, Feng L, et al. Optical detection of early damage in retinal ganglion cells in a mouse model of partial optic nerve crush injury. *Invest Ophthalmol Vis Sci*. 2016;57(13):5665–5671.
23. Huang X, Knighton R, Spector Y, Feuer W. Cytoskeletal alteration and change of retinal nerve fiber layer birefringence in hypertensive retina. *Curr Eye Res*. 2017;42(6):936–947.
24. Huang X, Knighton R, Spector Y, Qiao J, Kong W, Zhao Q. Reflectance spectrum and birefringence of the retinal nerve fiber layer with hypertensive damage of axonal cytoskeleton. *Invest Ophthalmol Vis Sci*. 2017;58(4):2118–2129.
25. Huang X, Bagga H, Greenfield D, Knighton R. Variation of peripapillary retinal nerve fiber layer birefringence in normal human subjects. *Invest Ophthalmol Vis Sci*. 2004;45(9):3073–3080.
26. Quigley HA, Dunkelberger GR, Green WR. Chronic human glaucoma causing selectively greater loss of large optic nerve fibers. *Ophthalmology*. 1988;95(3):357–363.
27. Quigley HA, Addicks EM, Green WR, Maumenee AE. Optic nerve damage in human glaucoma. II. The site of injury and susceptibility to damage. *Arch Ophthalmol*. 1981;99(4):635–649.

28. Jelinek H, Fernandez E. Neurons and fractals: how reliable and useful are calculations of fractal dimensions? *J Neurosci Methods*. 1998;81(1–2):9–18.
29. Ashimatey B, King B, Burns S, Swanson W. Evaluating glaucomatous abnormality in peripapillary optical coherence tomography enface visualisation of the retinal nerve fibre layer reflectance. *Ophthalmic Physiol Opt*. 2018;38(4):376–388.
30. Swanson WH, King BJ, Burns SA. Within-subject variability in human retinal nerve fiber bundle width. *PLoS One*. 2019;14(10):e0223350.
31. Ashimatey B, King B, Malinovsky V, Swanson W. Novel technique for quantifying retinal nerve fiber bundle abnormality in the temporal raphe. *Optom Vis Sci*. 2018;95(4):309–317.
32. Whitmore A, Libby R, John S. Glaucoma: thinking in new ways - a role for autonomous axonal self-destruction and other compartmentalised processes? *Prog Retin Eye Res*. 2005;24(6):639–662.
33. Nickells R. The long-term effects on the retina damaged by optic nerve axotomy. *Invest Ophthalmol Vis Sci*. 2015;56(10):6113.
34. Wong RO, Ghosh A. Activity-dependent regulation of dendritic growth and patterning. *Nat Rev Neurosci*. 2002;3(10):803–812.
35. Tian N. Development of retinal ganglion cell dendritic structure and synaptic connections. In: Kolb H, Fernandez E, Nelson R, eds. *Webvision: The Organization of the Retina and Visual System*. Salt Lake City, UT: University of Utah Health Sciences Center; 2012.
36. Erskine L, Herrera E. The retinal ganglion cell axon's journey: insights into molecular mechanisms of axon guidance. *Dev Biol*. 2007;308(1):1–14.
37. Seabrook T, Burbridge T, Crair M, Huberman A, Zoghbi H. Architecture, function, and assembly of the mouse visual system. *Annu Rev Neurosci*. 2017;40:499–538.
38. Fischer L, Culver D, Tennant P, et al. Amyotrophic lateral sclerosis is a distal axonopathy: evidence in mice and man. *Exp Neurol*. 2004;185(2):232–240.
39. Burgoyne C, Downs J, Bellezza A, Hart R. Three-dimensional reconstruction of normal and early glaucoma monkey optic nerve head connective tissues. *Invest Ophthalmol Vis Sci*. 2004;45(12):4388–4399.
40. Yang H, Reynaud J, Lockwood H, et al. The connective tissue phenotype of glaucomatous cupping in the. monkey eye - clinical and research implications. *Prog Retin Eye Res*. 2017;59:1–52.
41. Soto I, Pease M, Son J, Shi X, Quigley H, Marsh-Armstrong N. Retinal ganglion cell loss in a rat ocular hypertension model is sectorial and involves early optic nerve axon loss. *Invest Ophthalmol Vis Sci*. 2011;52(1):434–441.
42. Downs J, Yang H, Girkin C, et al. Three-dimensional histomorphometry of the normal and early glaucomatous monkey optic nerve head: neural canal and subarachnoid space architecture. *Invest Ophthalmol Vis Sci*. 2007;48(7):3195–3208.
43. Cordeiro M, Erskine L. Back to basics - ephrins, axonal guidance, neuroprotection and glaucoma. *Br J Ophthalmol*. 2007;91(9):1106–1106.
44. Stoeckli E. Understanding axon guidance: are we nearly there yet? *Development*. 2018;145(10):dev151415.
45. Varadarajan S, Huberman A. Assembly and repair of eye-to-brain connections. *Curr Opin Neurobiol*. 2018;53:198–209.
46. Fortune B, Cull G, Reynaud J, Wang L, Burgoyne C. Relating retinal ganglion cell function and retinal nerve fiber layer (RNFL) retardance to progressive loss of RNFL thickness and optic nerve axons in experimental glaucoma. *Invest Ophthalmol Vis Sci*. 2015;56(6):3936–3944.
47. Nikolaev A, McLaughlin T, O'Leary D, Tessier-Lavigne M. APP binds DR6 to trigger axon pruning and neuron death via distinct caspases. *Nature*. 2009;457(7232):981–989.
48. Libby R, Li Y, Savinova O, et al. Susceptibility to neurodegeneration in a glaucoma is modified by BAX gene dosage. *Plos Genetics*. 2005;1(1):17–26.
49. Nickells RW, Howell GR, Soto I, John SW. Under pressure: cellular and molecular responses during glaucoma, a common neurodegeneration with axonopathy. *Annu Rev Neurosci*. 2012;35:153–179.
50. Feng L, Zhao Y, Yoshida M, et al. Sustained ocular hypertension induces dendritic degeneration of mouse retinal ganglion cells that depends on cell type and location. *Invest Ophthalmol Vis Sci*. 2013;54(2):1106–1117.
51. Jakobs TC, Libby RT, Ben Y, John SW, Masland RH. Retinal ganglion cell degeneration is topological but not cell type specific in DBA/2J mice. *J Cell Biol*. 2005;171(2):313–325.
52. Minckler D. The organization of nerve-fiber bundles in the primate optic-nerve head. *Arch Ophthalmol*. 1980;98(9):1630–1636.
53. Shin ES, Sorenson C, Sheibani N. Diabetes and retinal vascular dysfunction. *J Ophthalmic Vis Res*. 2014;9(3):362–373.
54. Pi S, Hormel T, Wei X, et al. Monitoring retinal responses to acute intraocular pressure elevation in rats with visible light optical coherence tomography. *Neurophotonics*. 2019;6(4):041104.